atmosphere

MDPI

Article

Characteristics of the Evolution of Precipitation Particles during a Stratiform Precipitation Event in Liupan Mountains

Yujun Qiu [1,*], Nansong Feng [1], Ying He [1], Rui Xu [1,2] and Danning Zhao [3]

[1] Key Laboratory of Aerosol-Cloud-Precipitation of China Meteorological Administration, Nanjing University of Information Science & Technology, Nanjing 210044, China; 22301329@stu.cwxu.edu.cn (R.X.)
[2] School of Atmosphere and Remote Sensing, Wuxi University, Wuxi 214105, China
[3] Reading Academy, Nanjing University of Information Science & Technology, Nanjing 210044, China
* Correspondence: qyj@nuist.edu.cn

Abstract: This study utilizes comprehensive observational data from a stratiform mixed-cloud precipitation event in Liupan Mountains, combined with ground-based millimeter-wave cloud radar (CR), micro rain radar (MRR), and microwave radiometer (MR) data, to study the evolution characteristics and conversion efficiency of precipitation particles in the ice–water mixed layer, melting layer, and below these layers during the formation and dissipation of precipitation. The results show the following: (1) When precipitation particles occupy more than 20% of cloud layers detected by cloud radar, the ice–water mixed cloud layer descends and evolves into a precipitating cloud. (2) During surface precipitation periods, the proportion of raindrops forming precipitation was equivalent to that of small-scale precipitation particles in the cloud layers. The proportion of precipitation particles in the cloud layers with temperatures below 0 °C averaged 25%. Ice-phase particles within the bright band (BB) melted, coalesced, and grew into larger precipitation particles, increasing their proportion to 55%. (3) After surface precipitation ended, the water content and precipitation rate of the cloud layer were 60% and 52% of those during the precipitation process, respectively. The proportion of small-scale precipitation particles in the cloud layers was approximately half of that during the precipitation period. A large number of evaporated small-scale precipitation particles floated in the air layer below the clouds, occupying less than 6.0% of the cloud layers.

Keywords: cloud radar; micro rain radar; classification mask; particle identification; raindrop

check for updates

Citation: Qiu, Y.; Feng, N.; He, Y.; Xu, R.; Zhao, D. Characteristics of the Evolution of Precipitation Particles during a Stratiform Precipitation Event in Liupan Mountains. *Atmosphere* **2024**, *15*, 732. https://doi.org/10.3390/atmos15060732

Academic Editors: Alexander Kokhanovsky, Luca Lelli, Daniel Rosenfeld and Martin Gallagher

Received: 20 March 2024
Revised: 4 June 2024
Accepted: 17 June 2024
Published: 19 June 2024

1. Introduction

The transformation of cloud particles into precipitation particles represents a core aspect of cloud precipitation physics research [1–3], as the process involves complex physical phenomena, including condensation, coalescence, freezing, and melting, and remains fraught with many difficulties and challenges [3–6]. A principal characteristic of stratiform cloud precipitation involves the melting, aggregation, and fragmentation of ice-phase particles below the 0 °C layer [7–9]. Understanding the transition from cloud particles to precipitation particles and its efficiency is critical for precipitation forecasting, weather modification research, and precipitation parameterization [10–12].

Millimeter-wave cloud radar (CR) data provide the high temporal and spatial resolution features of cloud vertical structures with magnitudes of several decameters and a few seconds. Radar reflectivity, Doppler velocity, and spectral width measurements are also used to infer cloud water content and cloud particle size characteristics. For instance, Shupe [13] introduced a fuzzy logic method based on millimeter-wave cloud radar data to identify cloud phase states, and Shupe et al. [14] used this method to study polar cloud phase states. Song et al. [15] utilized CR observations from the third Tibetan Plateau Atmospheric Science Experiment conducted from 1 July to 31 August 2014, which studied cloud occurrence frequency, diurnal variations of cloud base, and cloud height. Zhao et al. [16,17]

used the same data to deduce water content in warm and ice clouds, while Qiu et al. [18] derived the water content in mixed clouds. However, due to the significant attenuation of CR in detecting precipitation particles, there are limitations in identifying and inverting microphysical quantities [19,20].

Micro rain radars (MRR) can accurately detect precipitation particles from light to moderate precipitation processes, providing data on precipitation intensity and particle velocities. Based on these data, additional information such as precipitation particle spectra and precipitation amount can be found. For example, Wen et al. [21] studied the statistical characteristics of raindrop size distributions observed in East China during the Asian summer monsoon season using 2D-video disdrometer and MRR data, highlighting that higher raindrop concentrations and smaller diameters are evident compared to monsoon precipitation at other locations in Asia. Das et al. [22] investigated the raindrop size distributions (DSDs) for different cloud types using data from the MRR and the Joss-Waldvogel Disdrometer (JWD) during the Indian summer monsoon (ISM) season from June to September for the period 2012–2015. Wang et al. [7] utilized stratiform precipitation data from a micro rain radar (MRR) located in Jinan city, Eastern China, to explore the bright band (BB) characteristics and hydrometeor classification. Garcia-Benadi et al. [23] introduced the RaProM methodology using MRR data to differentiate hydrometeor types. Foth et al. [24] presented two MRR-based approaches to distinguish stratiform and convective precipitation. However, since the maximum effective detection height of MRR is generally around 4 km, they cannot provide the vertical distribution of precipitation particles throughout the entire cloud layer. Therefore, combining CR and MRR can provide a way to study properties of cloud and rain [25].

The paper utilizes the field scientific experiment base at Liupan Mountains to conduct a comprehensive observation of a stratiform cloud precipitation event. By integrating ground-based millimeter-wave CR, MRR, and microwave radiometer (MR) data, the membership function for CR recognition of precipitation particles was identified. Based on this, precipitation particles throughout the cloud layers were identified using the fuzzy logic method. The study examined the spatiotemporal evolution characteristics and transformation efficiency of precipitation particles in the mixed-phase layer, melting layer, and below these layers during the precipitation formation and dissipation process. This research can provide a reference for precipitation forecasting, weather modification activities, and optimizing precipitation management efficiency.

2. Data and Methods

2.1. Study Area Introduction

LM is situated in the complex terrain under the massive geographical backdrop of the eastern Tibetan Plateau and the northwestern edge of the Loess Plateau. It is located in the central–southern part of Northwest China (Figure 1), and is one of the few elongated mountains with a northwest–southeast orientation (forming an angle of about 30° in the north–south direction). The ridges of the mountain rise above 2500 m, with the highest peak reaching 2942 m. The regional extent of LM is from 34.7 to 36.5° N latitude and 105.2 to 107° E longitude. For a detailed introduction, please refer to He et al. [9] and Xu et al. [26]. The LM orographic cloud field scientific experiment base constructed in this region has been used to conduct observations through a variety of remote sensing detection instruments, including CR, MRR, and MR.

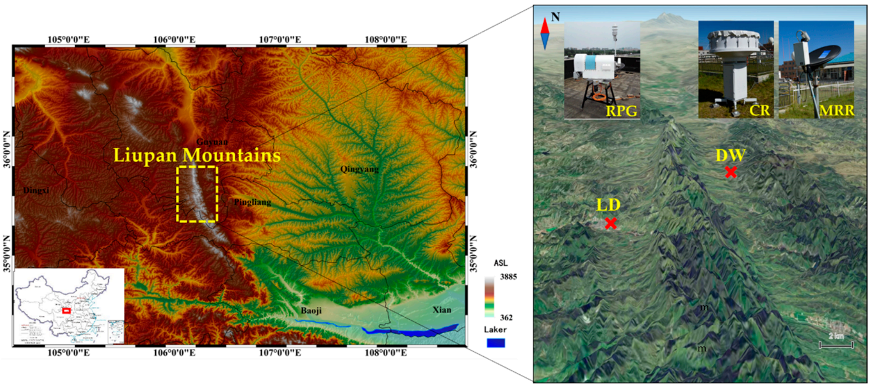

Figure 1. Geographical location and terrain of LMs; the distribution of two observation sites, Longde (LD, 2079 m ASL) and Dawan (DW, 1981 m ASL); and instrument scenes. The CR, MRR, and RPG denote Ka-band millimeter-wave cloud radar, K-band micro rain radar, and microwave radiometer from radiometer physics GmbH, respectively (study from [9,26]).

2.2. Data Description

This study examines a cloud precipitation event that occurred on 2 July 2021 in LMs, utilizing data from three types of ground-based remote sensors, including a K-band MRR, a Ka-band CR, and MR from radiometer physics GmbH (RPG). The CR and MRR were deployed at the DW observation station (1981 m above sea level (ASL)), while the MR was located at the LD observation station (35.37° N, 106.07° E, 2079 m ASL). He et al. [9] previously studied a mixed-phase cloud precipitation event in LMs using the aforementioned three data types.

The MRR is manufactured by METEK GmbH, Germany. It is a zenith-pointing frequency-modulated continuous-wave radar with an operational wavelength of 12.38 mm (24.23 GHz). The radar's temporal resolution is set to 1 min, and the spatial resolution is set to 150 m. Its maximum measurement range is up to 4650 m. MRR measurements include the equivalent reflectivity factor Ze (dBZ), the raindrop size distribution, and particle falling velocity. For detailed information on the data quality control of this instrument, please refer to Dang et al. [27].

The CR is another vertically pointing radar, produced by Xi'an Huateng Microwave Co., Ltd., Xi'an, China. This radar operates at a wavelength of 8.57 mm (35 GHz) and can detect cloud and precipitation profiles from 0.12 to 20 km with a temporal resolution of 5 s and a spatial resolution of 30 m. The CR measurements presented in this paper include equivalent reflectivity factor Ze (dBZ), Doppler spectrum, and spectral width—SW. The main specifications of the MRR and CR are summarized in Table 1 of He et al. [9]. Information on data quality control and applications of this instrument is available in the study by Tian et al. [28].

The MR is located at the Longde National Meteorological Observatory in LMs and is a ground-based microwave radiometer of the RPG-HATPRO type from RPG, Germany. This instrument employs multi-channel parallel measurement techniques, offering advantages such as high temporal and spatial resolution and all-weather and full-time observation capabilities. It enables the real-time, continuous monitoring and acquisition of atmospheric temperature and humidity profiles, as well as data products such as atmospheric water vapor content, within a 0–10 km range. For this article, we utilized temperature profile data with a temporal resolution of 1 min, divided into 93 vertical layers. For detailed explanations, please consult the station personnel's work [29,30].

2.3. Cloud Particle and Precipitation Particle Identification Methods

Firstly, the vertical layers and time of the MRR and CR data are matched. Then, the CR data with detection signals from the MRR at the same time points as the precipitation particle data are selected. Additionally, data with no detection signals from the MRR but with detection signals from the CR are considered as cloud particle data. In this paper, particles within a cloud that can be detected by the MRR in terms of scale are referred to as precipitation particles. Particles that can detach from the cloud and undergo free fall are termed raindrops. Here, the term "precipitation particles" refers to particles that have not yet grown into raindrops and are smaller than raindrops; raindrops are larger-scale precipitation particles.

The CR's detection quantities, including reflectivity factor, Doppler velocity, and spectral width, do not uniquely respond to different hydrometeors. Based on the results of Shupe [13], we employ fuzzy logic to classify cloud droplets and precipitation particles. The applied membership functions are determined according to the following steps:

(1) Within the range of the reflectivity factor, Doppler velocity, and spectral width where only cloud droplets are present, the membership functions for each parameter of cloud droplets are set to 1, while the membership function values for precipitation particles are set to 0. Conversely, within the range of the reflectivity factor, Doppler velocity, and spectral width where only precipitation particles are present, the membership function values for precipitation particles are set to 1, and the membership function values for cloud droplets are set to 0.

(2) Within the range of the reflectivity factor, Doppler velocity, and spectral width where both cloud droplets and precipitation particles are present, the membership function values for cloud droplets linearly decrease from 1 to 0 across the parameter range, while for precipitation particles they linearly increase from 0 to 1.

(3) For a given height layer and specific time point, the membership function value f for cloud droplets is determined by the corresponding membership function value fi (where i = 1, 2, 3 correspond to reflectivity factor, Doppler velocity, and spectral width, respectively). It is expressed as follows:

$$\mathrm{f} = \sum\nolimits_{\mathrm{i}=1}^{3} \mathrm{f_i} \tag{1}$$

From (1), the membership function values f for cloud droplets, precipitation particles, and raindrops can be obtained. The particles with the highest f value are identified as the particle type corresponding to that height layer and time.

2.4. The Proportion of Cloud Particles and Precipitation Particles

Identify cloud droplets and precipitation particles and assign them to each cloud radar (CR) altitude layer, obtaining samples C with only cloud droplets, P with precipitation particles, and R with raindrops at different altitudes. Calculate the total number of cloud layers under conditions C, P, and R, denoted by $\mathrm{N_C}$, $\mathrm{N_P}$, and $\mathrm{N_R}$, respectively. The proportions of these cloud layers within the total cloud layers, represented by $\mathrm{X_C}$, $\mathrm{X_P}$, and $\mathrm{X_R}$, are computed using Equations (2)–(4).

$$\mathrm{X_C} = \frac{\mathrm{N_c}}{\mathrm{N_C} + \mathrm{N_P} + \mathrm{N_R}} * 100\% \tag{2}$$

$$\mathrm{X_P} = \frac{\mathrm{N_P}}{\mathrm{N_C} + \mathrm{N_P} + \mathrm{N_R}} * 100\% \tag{3}$$

$$\mathrm{X_R} = \frac{\mathrm{N_R}}{\mathrm{N_C} + \mathrm{N_P} + \mathrm{N_R}} * 100\% \tag{4}$$

Within the studied time series, $\mathrm{X_C}$ represents the proportion of cloud layers with only cloud droplets to the total number of cloud layers, $\mathrm{X_P}$ denotes the proportion of cloud layers with precipitation particles to the total number of cloud layers, and $\mathrm{X_R}$ indicates the proportion of cloud layers with raindrops to the total number of cloud layers.

3. Results

3.1. Overview of Cloud Precipitation Processes

During the cloud precipitation event that occurred on 2 July 2021, both the CR (cloud radar) and the MRR (micro rain radar) observed a bright band (BB) from 4:30 to 10:00 (stage2), as seen in Figure 2. Following the method of Wang et al. [7], the BB appeared at an altitude layer of 1.35 to 1.95 km, where the maximum reflectivity factor detected by the CR and the maximum precipitation rate detected by the MRR were both present within the BB. The average temperature of the BB, as detected by the MRR, ranged between 4.0 and 5.6 °C. During this period, the MRR detected a substantial amount of precipitation particles extending from the clouds down to the ground. The maximum Doppler velocity, the maximum velocity spectral width detected by the CR, and the maximum fall speed detected by the MRR all occurred just below the BB. It is worth noting that in the pre-precipitation period from 0:00 to 4:30 (stage1), the CR detected a minimum temperature of approximately −40 °C inside the cloud layer, with the temperature at the cloud base higher than −10 °C, suggesting that the cloud droplets were in a mixed phase of ice and water. The cloud base height decreased in stage2, with the melting of ice particles, hence the appearance of the bright band. Surface precipitation was observed during stage2, with total surface precipitation amounting to 1.9 mm for the period, indicating that this was a weak precipitation event associated with stratiform mixed clouds.

During the stage2 period, the MRR (micro rain radar) detected a large number of precipitation particles, and during the stage1 and stage3 periods, it also detected fewer millimeter-sized precipitation particles below the cloud base. The precipitation rate during stage1 was negligible, while during stage3, a high precipitation rate of 13.3 mm/h was observed, but the surface precipitation was 0 (Figure 3b). The time series of surface temperature and relative humidity seen in Figure 3d indicate that, following the end of the precipitation, the surface temperature gradually increased from 11.6 °C, reaching 15.4 °C at noon, while the high relative humidity persisted until 11:00 with an average of 90%, and then gradually decreased from 81% at noon to 43% by 16:00. This implies that during stage3, the temperature of the atmospheric layer was high and evaporation was intense, which resulted in the precipitation particles detaching from the cloud base being evaporated while the temperature rose, causing them to float within the atmospheric layer.

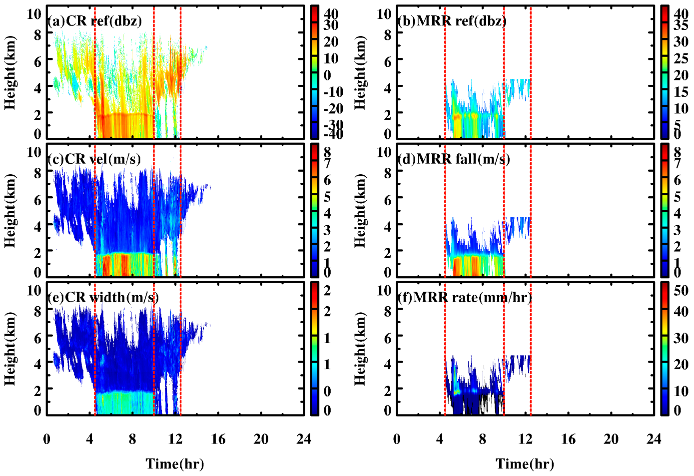

Figure 2. The vertical distribution of parameters was measured by cloud radar (CR) and micro rain radar (MRR) during the precipitation event in LMs on 2 July 2021. The CR data include (**a**) reflectivity factor, (**c**) Doppler velocity, and (**e**) spectrum width, while the MRR data cover (**b**) reflectivity factor, (**d**) fall velocity, and (**f**) rain rate. The time segments delineated by red vertical dashed lines correspond to the pre-precipitation period (stage1), the precipitation event (stage2), and the post-precipitation period (stage3), respectively.

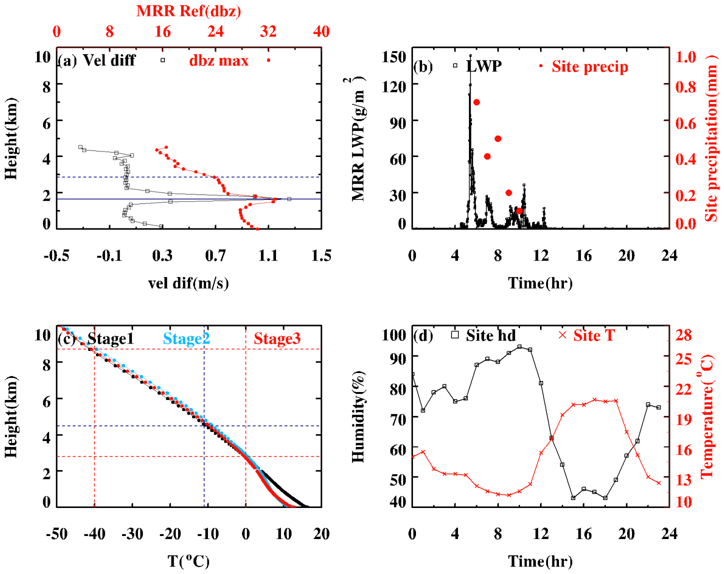

Figure 3. The precipitation process in LMs on 2 July 2021 featured (**a**) the variability of fall velocity between two adjacent altitude layers and the distribution of the maximum reflectivity factor with height measured by MRR, (**b**) the liquid water content detected by MRR and the hourly precipitation amount measured at the ground-based observation station, (**c**) the temperature profile measured by MR, and (**d**) the distribution of relative humidity and temperature over time as measured at the ground-based observation station. In (**a**), the blue horizontal dashed line represents the altitude layer where the average temperature is 0 °C, and the solid blue line indicates the altitude layer where the changes in fall velocity and the strongest MRR signals are observed.

From the above, it is concluded that this precipitation event belongs to a weak precipitation process of stratiform mixed clouds. Both before and after surface precipitation, precipitation particles float in the lower atmosphere below the cloud. After surface precipitation, the cloud still maintains a relatively high precipitation rate.

3.2. Characteristics of Precipitation Particles Detected by MRR

The MRR can detect precipitation particles in the sub-millimeter and millimeter scales within cloud layers and raindrops below clouds. However, the maximum detection altitude of the MRR is 4.5 km, where the lowest average temperature at this level is approximately −11 °C (Figure 3c), and the average 0 °C level is around 2.7 km. As observed in Figure 4, within the mixed layer, the maximum reflectivity factor, the settling velocity, and the precipitation rate rapidly increase with decreasing altitude, which implies that cloud particle size quickly grows during the descent.

The liquid water content and precipitation rate during stage2 are 1.7 and 1.9 times those during stage3, respectively, while the average mass diameter of hydrometeors is 1.5 and 1.1 times that during stage1 and stage3, respectively. It is noteworthy that the maximum rate, mean rate, and mean liquid water content between the cloud layer with an average temperature of 0 °C and the lowest temperature layer of the bright band decrease rapidly with height. The mass-weighted average diameter (Mde) increases rapidly, implying a rapid decrease in cloud particles and an increase in precipitation particles, mainly involving snow crystal melting and aggregation processes [31]. Ice-phase particles gradually melt and merge with cloud droplets to form larger precipitation particles.

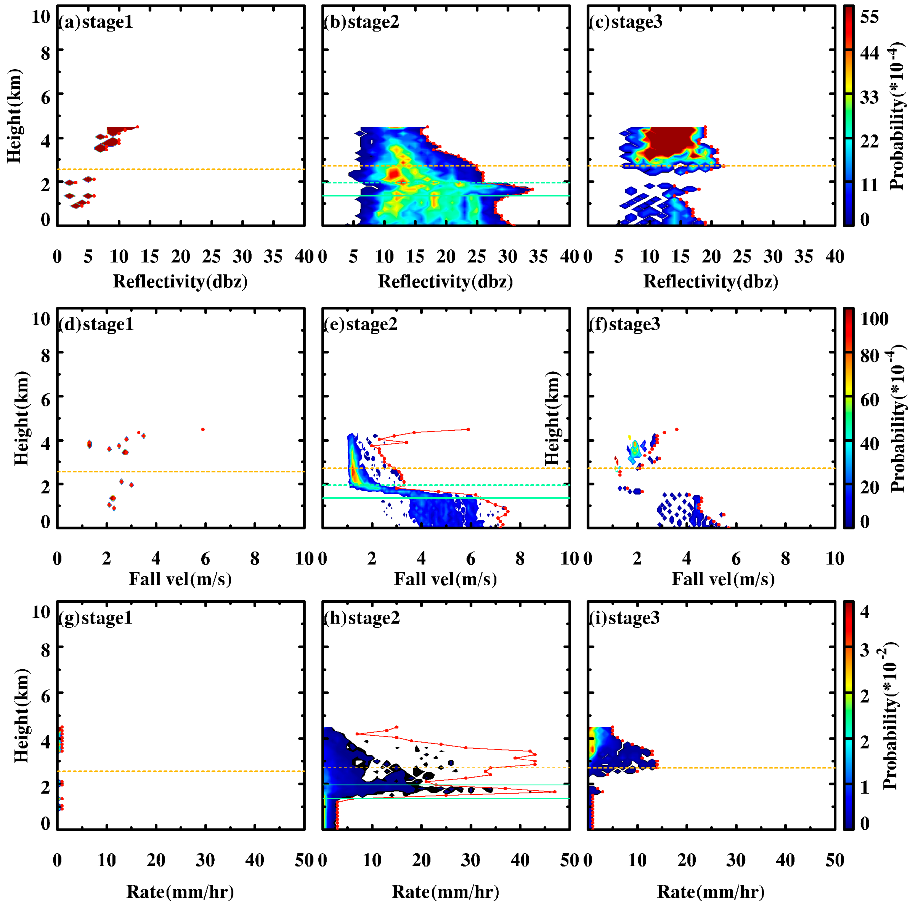

Figure 4. The probabilistic distribution of MRR detections at various vertical heights for three different stages related to precipitation on 2 July 2021, in LMs during the pre-precipitation period (stage1), the precipitation event (stage2), and the post-precipitation period (stage3). The figures are divided as follows: (**a**–**c**) show the reflectivity factor; (**d**–**f**) depict the fall velocity; and (**g**–**i**) represent the precipitation rate. Specifically, (**a**,**d**,**g**) correspond to the pre-precipitation period (stage1); (**b**,**e**,**h**) correspond to the period during the precipitation (stage2); and (**c**,**f**,**i**) relate to the stage after the precipitation (stage3). The red dots connected by lines represent the maximum values of each physical quantity at their respective altitude levels. The yellow horizontal dashed lines indicate the heights where the average temperature is 0 °C, whereas the areas between the blue dashed lines and the blue solid lines correspond to the bright band layer.

According to Figure 5, on average, the precipitation amount and precipitation rate during the pre-precipitation period (stage1) are negligible, being an order of magnitude smaller than those observed during the precipitation event (stage2) and the post-precipitation period (stage3). The liquid water content (LWC) and the precipitation rate during stage2 are, respectively, 1.7 and 1.9 times those of stage3, while the average mass diameter of hydrometeors during stage2 is 1.5 times that of stage1 and 1.1 times that of stage3. It is important to note that, from the elevation layer with an average temperature of 0 °C to the lowest temperature layer of the BB, the maximum rate, average rate, and average LWC all decrease rapidly with decreasing altitude, while the average mass-weighted mean diameter (Mde) increases rapidly (as illustrated in Figure 5b,c). This mainly involves snow crystal melting and aggregation processes, ice-phase particles gradually melt and merge with cloud droplets to grow into larger precipitation particles [31].

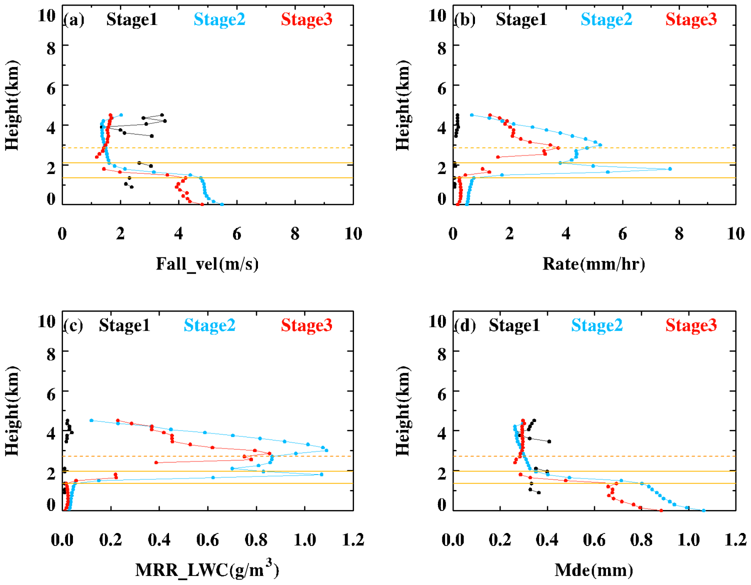

Figure 5. The characteristics of the precipitation process in LMs on 2 July 2021, during three different stages, with: (**a**) fall velocity, (**b**) precipitation rate, (**c**) liquid water content, and (**d**) mass-weighted mean diameter. The black, blue, and red dotted lines in the figures represent the stage before precipitation (stage1), the stage during precipitation (stage2), and the stage after precipitation (stage3), respectively. The yellow horizontal dashed line indicates the altitude corresponding to the 0 °C temperature level, while the layer outlined by the yellow dashed line represents the bright band.

Within the BB, the maximum reflectivity factor, the maximum rate, the average rate, and the average LWC increase with decreasing altitude to reach peak values, suggesting that the ice-phase particles within the BB have fully melted, and the quantity of liquid particles has rapidly increased. This enhances the collision–coalescence process between particles, leading to a rapid increase in the size of precipitation particles. This is confirmed by the average Mde value, which rapidly increases with decreasing altitude and is shown in Figure 5d. The rapid decrease in LWC at the lower levels of the BB might be due to a reduction in the number of precipitation particles, with the maximum reflectivity factor also rapidly decreasing at this layer. Below the BB, within the height layer, the average rate and LWC values are small and show little change, while the settling velocity and mass-weighted diameter gradually increase with decreasing altitude. This indicates that the precipitation particles have evolved from their cloud phase into raindrops.

3.3. Precipitation Particle Identification based on CR

Using millimeter-wave cloud radar and micro rain radar detection data, three types of samples, C (cloud drops only), P (precipitation particles), and R (raindrops), were selected. The probability distributions of reflectivity factor (Re), Doppler velocity (V), and spectral width (W) for cloud particles and precipitation particles as detected by the cloud radar were determined (Figure 6).

From the comparison of the probability distributions of Re for the C, P, and R samples shown in Figure 6, it was found that for layers with only cloud drops, the reflectivity factor ranges from −40 dBZ to −10 dBZ with the maximum reflectivity factor at 0 dBZ. The minimum reflectivity factor for layers with precipitation particles starts at −10 dBZ, with over 80% appearing in the 10–25 dBZ range. The minimum reflectivity factor for raindrops is at 5 dBZ. Comparing the V probability distributions, only for cloud drops does the cloud layer’s Doppler velocity range from 0 m/s to 1.0 m/s, with the maximum Doppler velocity at 5 m/s. The Doppler velocity for precipitation particles has a minimum of 1 m/s and a maximum of 5 m/s, with the highest frequency at 1.8 m/s. Additionally, the minimum Doppler velocity for raindrops is 3.2 m/s. In terms of the probability distribution for the

Doppler spectral width, cloud layers with only cloud drops have a W distribution less than or equal to 0.1 m/s, with 90% probability concentrated within a range smaller than 0.5 m/s. The minimum and maximum spectral widths for precipitation particles are 0.2 m/s and 1.2 m/s, respectively, mainly concentrated in the 0.3–0.6 m/s range. The minimum spectral width for signals with raindrops is 0.6 m/s.

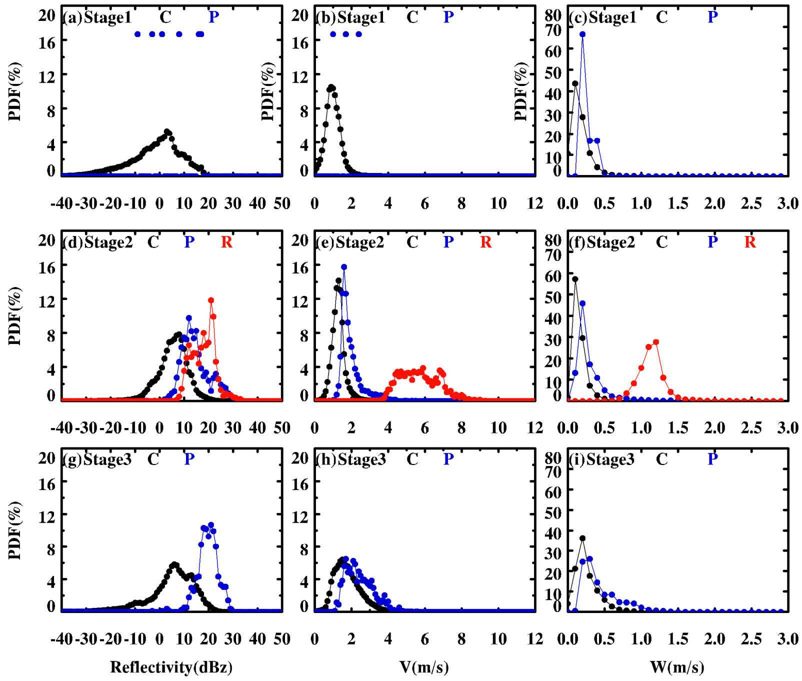

Figure 6. The probability distribution of cloud radar detection parameters under the conditions of C, P, and R during three different periods: before, during, and after the precipitation on 2 July 2021, in LMs. The figures are categorized as follows: (**a**,**d**,**g**) present the radar reflectivity factor; (**b**,**e**,**h**) display Doppler velocity; and (**c**,**f**,**i**) illustrate spectrum width. Specifically, (**a**–**c**) correspond to the period before the precipitation (stage1); (**d**–**f**) correspond to the period during the precipitation (stage2); and (**g**–**i**) correspond to the period after the precipitation (stage3).

Based on the characteristic distributions of CR parameters for cloud drops and precipitation particles, membership functions for each parameter were obtained (see Table 1). It should be noted that the temperature in the cloud layer was below 0 °C, and the precipitation particles were primarily in the form of ice crystals and snowflakes, and raindrops primarily occur in the atmospheric layer below the cloud base during the stage2 time period. As seen in Figure 6, the upper limits for the corresponding reflectivity factor, Doppler velocity, and spectral width for raindrops are all higher than those for precipitation particles within the cloud. This suggests that raindrops result from the growth of precipitation particles such as snowflakes and ice–water mixtures through physical processes like melting and coalescence.

3.4. Spatiotemporal Evolution Characteristics of Precipitation Particles

Based on the membership functions provided in Table 1, the distributions of C, P, and R for different height layers at various time points were determined (see Figure 7). Statistics reveal that the mean proportion of X_C across all height layers at the same time are ranked from largest to smallest as stage1, stage2, and stage3, with respective values of 81.7%, 47.5%, and 38.2%. In other words, when X_P is around 20%, non-precipitating clouds will evolve into precipitating clouds, resulting in precipitation at the ground level. During stage2, X_P reaches 53.5%, with X_R accounting for 25.1%, a proportion approximately equal to that of precipitation particles within the cloud. It should be mentioned that during stage3, the proportion of precipitation particles rises to 57.2%, which is consistent with the higher precipitation rate and LWC values shown in Figure 5. During the stage3 period, the proportion of particles that have grown to the size of raindrops is about 4.6%; however, the observed ground precipitation is 0 mm. Combined with the temperature and humidity distribution characteristics in Figure 4, this indicates that, at this time, due to high temperatures and strong evaporation, raindrops are easily evaporated into smaller precipitation particles that linger in the air.

Table 1. Membership functions of cloud droplets, precipitation particles, and raindrops within the detection ranges of cloud radar reflectivity factor, Doppler velocity, and spectrum width.

	Reflectivity Factor		**Doppler Velocity**		**Spectrum Width**	
	Range (dbz)	**Functions**	**Range (m/s)**	**Functions**	**Range (m/s)**	**Functions**
Cld_Drops	[−40,−10)	1	[0,1)	1	[0,0.1)	1
	[−10,0)	(0 − Re)/10.0	[1,5)	(5 − v)/4	[0.1,0.5)	(0.5 − w)/0.4
	[0,50]	0	[5,11)	0	[0.5,2.3)	0
Precip_Particles	[−40,−10)	0	[0,1)	0	[0,0.1)	0
	[−10,10)	(10 − Re)/20.0	[1.0,1.8)	(v − 1.0)/0.8	[0.2,0.5)	(w − 0.2)/0.3
	[10,25)	1	[1.8,5.0)	(5.0 − v)/3.2	[0.5,1.5)	(1.5 − v)/1.0
			[5.0,11)	0	[1.5,2.3)	0
Raindrops	[−40,5)	0	[0,3.2)	0		
	[5,25)	(Re − 5)/20.0	[3.2,5.0)	(v − 3.2)/1.8	[0.6,1.5)	(w − 0.6)/0.9
	[25,50)	1	[5.0,11)	1	[1.5,2.3)	1

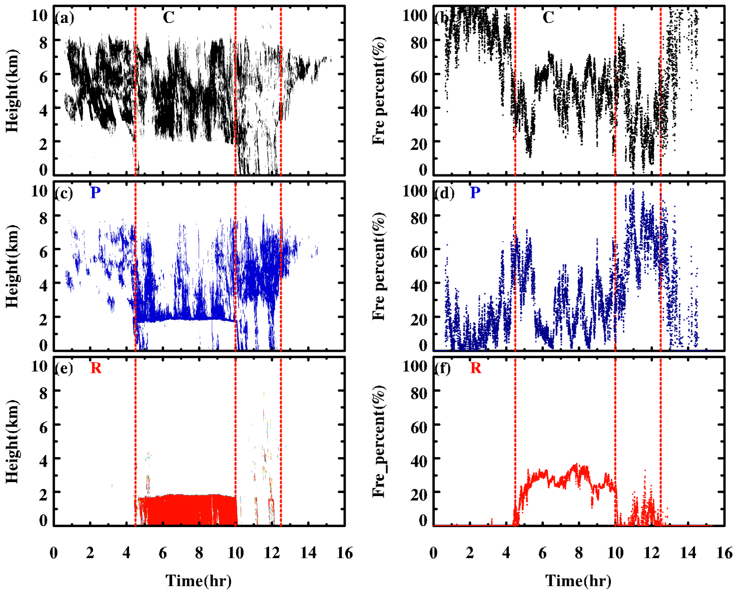

Figure 7. The distribution characteristics of cloud particles during the cloud precipitation process at Dawan Station in LMs on 2 July 2021. The figures are organized as follows: (**a**,**c**,**e**) show the height distribution under the conditions of C, P, and R, respectively; (**b**,**d**,**f**) represent the time series of X_C, X_P, and X_R, respectively. The three red dashed lines at 4:30, 10:00, and 12:30 correspond to the times before precipitation, at the end of precipitation, and after precipitation, respectively.

From the average distribution of X_C, X_P, and X_R across the vertical height layers during the three time periods (see Figure 8), we can see that during stage1, the mixed cloud layer is thick, with precipitation particles present at different heights within the cloud. The proportion of layers containing precipitation particles reaches higher values in the middle part of the cloud, where the average temperature is about −15 °C, indicating that the cloud droplets are in a mixed phase of ice and water. The mean value of X_C within the cloud is

5.0 times that of X_P, which corresponds with the results shown in Figure 7d, meaning that when the proportion of precipitation particles X_P reaches 17–20%, the cloud base starts to descend, gradually evolving into the precipitating cloud of stage2. It should be noted that the CR has three detection modes targeted at the near-surface, precipitation, and cirrus clouds. The vertical profiles of the radar reflectivity factor, Doppler velocity, and spectrum width are pieced together by these three modes, with the joints located at 1.02 km and 3.21 km, respectively. There are discontinuities at these two height layers for the profiles of the three detection parameters, but they do not impact the comparison of X_C, X_P, and X_R.

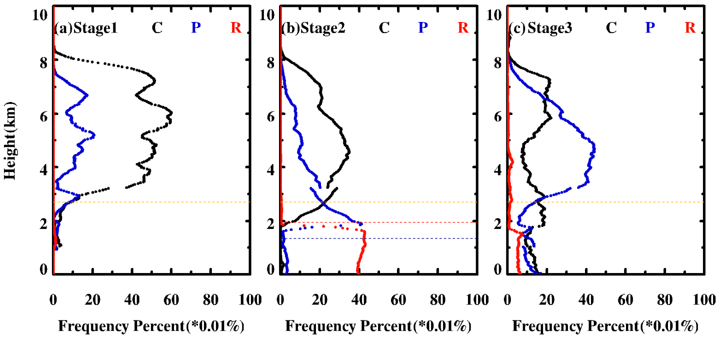

Figure 8. The average profiles of X_C, X_P, and X_R under conditions C, P, and R during three cloud precipitation periods at Dawan Station in LMs on 2 July 2021. The sub-figures are as follows: (**a**) stage1, (**b**) stage2, and (**c**) stage3.

Due to the influence of temperature, as the cloud develops to stage2 and the cloud base descends, the temperature rises above 0 °C. Cloud droplets in a mixed phase of ice and water undergo physical processes such as melting and coalescence, leading to the formation of precipitation particles. The number of cloud layers containing precipitation particles increases with height according to a logarithmic rule, with a greater increase below the 0 °C layer. A bright band (BB) appears at the cloud base, and all the precipitation particles below the bright band layer are transformed into raindrops. Above the 0 °C layer height, within the cloud, X_C is 3.0 times that of X_P. Compared to stage1, the proportion of X_P within this cloud layer has increased by 13%. The X_P above the cloud base and up to the 0 °C layer height is 1.2 times that of X_C. This layer represents the cloud layer where cloud droplet size rapidly grows into raindrop size. Below the cloud base, the air layer is filled with raindrops, with X_R being approximately 5.7 times that of X_P.

After the cessation of surface precipitation, the precipitation particles X_P within the cloud layers above 0 °C remain relatively high, approximately 2.0 times that of X_C, averaging 66% across all cloud layers. X_C and X_P dramatically decrease from below the 0 °C layer to above the 2 km height layer, with X_C being 1.2 times that of X_P, and 8.7% of the particles are of raindrop size at this height layer. Combining ground meteorological observation data, it is determined that the particle sizes at this layer do not produce surface precipitation. This is primarily due to the influence of higher temperatures causing evaporation. The proportions of cloud droplets and undeposited large-scale particles is comparable in the cloud layers.

4. Conclusions

This study utilizes various remote sensing data, including millimeter-wave cloud radar, micro rain radar, microwave radiometer, and ground-based meteorological observations at the Liupan Mountain Terrain Cloud Field Scientific Experiment Base, to establish a fuzzy membership function using CR to identify cloud droplets, precipitation particles, and raindrops. The spatiotemporal evolution characteristics of precipitation particles during a weak precipitation process in a stratiform cloud are investigated. The main conclusions are as follows:

(1) The proportions of small-scale precipitation particles of cloud layers before, during, and after precipitation periods are 18.0%, 27.4%, and 57.2%, respectively. During precipitation, particles sink below the cloud base, ice particles melt and form bright bands, and maximum sinking velocities and precipitation rates occur in the bright bands. After surface precipitation ends, the cloud's water content and precipitation rate are 60% and 52% of those during precipitation periods, respectively.

(2) During precipitation, ice-phase particles below the 0 °C altitude layer melt, merge with cloud droplets, and grow into larger precipitation particles, with low-level precipitation particles evolving into raindrops within the bright bands. The proportion of small-scale precipitation particles and raindrops of cloud layers is similar, with small-scale precipitation particles in ice–water mixed layers accounting for approximately 25%, and raindrops approximately 25.1% of cloud layers.

(3) After surface precipitation ends, small-scale precipitation particles in ice–water mixed layers account for approximately 66% of cloud layers. Below the 0 °C altitude layer, small-scale precipitation particles that evaporate due to high temperatures float, occupying approximately 6% of cloud layers, which is about 20% of the precipitation period.

Author Contributions: Conceptualization, Y.Q.; methodology, Y.Q.; validation, Y.Q. and N.F.; formal analysis, Y.Q.; investigation, Y.Q.; resources, Y.Q.; data curation, Y.Q., N.F. and Y.H.; writing—original draft preparation, Y.Q.; writing—review and editing, Y.Q.; visualization, Y.Q., R.X. and D.Z.; supervision, Y.Q.; project administration, Y.Q.; funding acquisition, Y.Q. All authors have read and agreed to the published version of the manuscript.

Funding: This research was funded by the National Natural Science Foundation of China, grant number 42075073 and 42075077, and key subjects of soft science in bureau of meteorology with grant number 2021ZDIANXM22.

Institutional Review Board Statement: Not applicable.

Informed Consent Statement: Not applicable.

Data Availability Statement: The data presented in this study are available on request from the corresponding author. The data are not publicly available due to privacy.

Acknowledgments: We appreciate the data provided by the Key Laboratory of Monitoring, Early Warning and Risk Management of Agricultural Meteorological Disasters with Special Characteristics in Dry Areas of the China Meteorological Administration (CMA) and the Key Laboratory of Meteorological Disaster Prevention and Mitigation in Ningxia.

Conflicts of Interest: The authors declare no conflict of interest.

References

1. McFarquhar, G.M.; Um, J.; Jackson, R. Small cloud particle shapes in mixed-phase clouds. *J. Appl. Meteorol. Climatol.* **2013**, *52*, 1277–1293. [CrossRef]
2. Kiliani, J.; Baumgarten, G.; Lübken, F.-J.; Berger, U. Impact of particle shape on the morphology of noctilucent clouds. *Atmos. Chem. Phys.* **2015**, *15*, 12897–12907. [CrossRef]
3. Morrison, H.; van Lier-Walqui, M.; Fridlind, A.M.; Grabowski, W.W.; Harrington, J.Y.; Hoose, C.; Korolev, A.; Kumjian, M.R.; Milbrandt, J.A.; Pawlowska, H.; et al. Confronting the challenge of modeling cloud and precipitation microphysics. *J. Adv. Model. Earth Syst.* **2020**, *12*, e2019MS001689. [CrossRef] [PubMed]
4. Baker, M.B. Cloud microphysics and climate. *Science* **1997**, *276*, 1072–1078. [CrossRef]
5. Ceppi, P.; Brient, F.; Zelinka, M.D.; Hartmann, D.L. Cloud feedback mechanisms and their representation in global climate models. *WIREs Clim. Chang.* **2017**, *8*, e465. [CrossRef]
6. Lin, L.; Liu, X.; Fu, Q.; Shan, Y. Climate impacts of convective cloud microphysics in NCAR CAM5. *J. Clim.* **2023**, *36*, 3183–3202. [CrossRef]
7. Wang, H.; Lei, H.; Yang, J. Microphysical processes of a stratiform precipitation event over eastern China: Analysis using micro rain radar data. *Adv. Atmos. Sci.* **2017**, *34*, 1472–1482. [CrossRef]
8. Heymsfield, A.J.; Bansemer, A.; Theis, A.; Schmitt, C. Survival of snow in the melting layer: Relative humidity influence. *J. Atmospheric Sci.* **2021**, *78*, 1823–1845. [CrossRef]

9. He, Y.; Shu, Z.; Zheng, J.; Jia, X.; Qiu, Y.; Deng, P.; Yan, X.; Lin, T.; Dang, Z.; Lu, C. A Comparative Study on the Vertical Structures and Microphysical Properties of a Mixed Precipitation Process over Different Topographic Positions of the Liupan Mountains in Northwest China. *Atmosphere* **2022**, *14*, 44. [CrossRef]
10. Zhang, G.; Sun, J.; Brandes, E.A. Improving parameterization of rain microphysics with disdrometer and radar observations. *J. Atmospheric Sci.* **2006**, *63*, 1273–1290. [CrossRef]
11. Ashfaq, M.; Ghosh, S.; Kao, S.; Bowling, L.C.; Mote, P.; Touma, D.; Rauscher, S.A.; Diffenbaugh, N.S. Near-term acceleration of hydroclimatic change in the western U.S. *J. Geophys. Res. Atmos.* **2013**, *118*, 10676–10693. [CrossRef]
12. Ma, Z.; Liu, Q.; Zhao, C.; Li, Z.; Wu, X.; Chen, J.; Yu, F.; Sun, J.; Shen, X. Impacts of transition approach of water vapor-related microphysical processes on quantitative precipitation forecasting. *Atmosphere* **2022**, *13*, 1133. [CrossRef]
13. Shupe, M.D. A ground-based multisensor cloud phase classifier. *Geophys. Res. Lett.* **2007**, *34*, L22809. [CrossRef]
14. Shupe, M.D.; Walden, V.P.; Eloranta, E.; Uttal, T.; Campbell, J.R.; Starkweather, S.M.; Shiobara, M. Clouds at Arctic atmospheric observatories. Part I: Occurrence and macrophysical properties. *J. Appl. Meteorol. Climatol.* **2011**, *50*, 626–644. [CrossRef]
15. Song, X.; Zhai, X.; Liu, L.; Wu, S. Lidar and ceilometer observations and comparisons of atmospheric cloud structure at nagqu of tibetan plateau in 2014 Summer. *Atmosphere* **2017**, *8*, 9. [CrossRef]
16. Zhao, C.; Liu, L.; Wang, Q.; Qiu, Y.; Wang, W.; Wang, Y.; Fan, T. Toward Understanding the Properties of High Ice Clouds at the Naqu Site on the Tibetan Plateau Using Ground-Based Active Remote Sensing Measurements Obtained during a Short Period in July 2014. *J. Appl. Meteorol. Clim.* **2016**, *55*, 2493–2507. [CrossRef]
17. Zhao, C.; Liu, L.; Wang, Q.; Qiu, Y.; Wang, Y.; Wu, X. MMCR-based characteristic properties of non-precipitating cloud liquid droplets at Naqu site over Tibetan Plateau in July 2014. *Atmos. Res.* **2017**, *190*, 68–76. [CrossRef]
18. Qiu, Y.; Lu, C.; Luo, S. Tibetan Plateau Cloud Structure and Cloud Water Content Derived from Millimeter Cloud Radar Observations in Summer. *Pure Appl. Geophys.* **2019**, *176*, 1785–1796. [CrossRef]
19. Kollias, P.; Rémillard, J.; Luke, E.; Szyrmer, W. Cloud radar Doppler spectra in drizzling stratiform clouds: 1. Forward modeling and remote sensing applications. *J. Geophys. Res.* **2011**, *116*, D13201. [CrossRef]
20. Al-Sakka, H.; Boumahmoud, A.-A.; Fradon, B.; Frasier, S.J.; Tabary, P. A new fuzzy logic hydrometeor classification scheme applied to the French X-, C-, and S-band polarimetric radars. *J. Appl. Meteorol. Clim.* **2013**, *52*, 2328–2344. [CrossRef]
21. Wen, L.; Zhao, K.; Zhang, G.; Xue, M.; Zhou, B.; Liu, S.; Chen, X. Statistical characteristics of raindrop size distributions observed in East China during the Asian summer monsoon season using 2-D video disdrometer and Micro Rain Radar data. *J. Geophys. Res. Atmos.* **2016**, *121*, 2265–2282. [CrossRef]
22. Das, S.K.; Konwar, M.; Chakravarty, K.; Deshpande, S.M. Raindrop size distribution of different cloud types over the Western Ghats using simultaneous measurements from Micro-Rain Radar and disdrometer. *Atmos. Res.* **2017**, *186*, 72–82. [CrossRef]
23. Garcia-Benadi, A.; Bech, J.; Gonzalez, S.; Udina, M.; Codina, B.; Georgis, J.-F. Precipitation type classification of micro rain radar data using an improved doppler spectral processing methodology. *Remote Sens.* **2020**, *12*, 4113. [CrossRef]
24. Foth, A.; Zimmer, J.; Lauermann, F.; Kalesse-Los, H. Evaluation of micro rain radar-based precipitation classification algorithms to discriminate between stratiform and convective precipitation. *Atmos. Meas. Tech.* **2021**, *14*, 4565–4574. [CrossRef]
25. Ojo, J.S.; Daodu, O.O.; Ojo, O.L. Analysis of vertical profiles of precipitable liquid water content in a tropical climate using micro rain radar. *J. Geosci. Environ. Prot.* **2019**, *7*, 140–155. [CrossRef]
26. Xu, R.; Qiu, Y. The Difference in Cloud Water Resources and Precipitation on the Eastern and Western Sides of the Liupan Mountains Caused by Topographic Effects. *Atmosphere* **2023**, *14*, 1502. [CrossRef]
27. Dang, Z.L.; Chang, Z.L.; Cao, N.; Wang, M. Precision Evaluation of Micro Rain Radar Observations during a Stratiform Cloud Precipitation Process. *Ningxia Eng. Technol.* **2021**, *20*, 8–11+17. (In Chinese)
28. Tian, L.; Sang, J.R.; Yao, Z.Y.; Chang, Z.L.; Shu, Z.L. Preliminary analysis of cloud macro characteristics over the Liupan mountain based on Ka-band cloud radar. *J. Meteorol. Environ.* **2021**, *37*, 84–90. (In Chinese)
29. Sun, Y.Q.; Tang, D.Z.; Sang, J.R.; Wang, Y.; Lv, J.J. Quality control method and efficiency analysis on temperature data by RPG_HATPRO_G4 type ground-based microwave radiometer. *Arid. Land Geogr.* **2019**, *42*, 1282–1290. (In Chinese)
30. Tian, L.; Sang, J.R.; Yao, Z.Y.; Chang, Z.L.; Shan, X.L.; Cao, L.; Sun, Y.Q. Characteristics of atmosphereic water vapor and liquid water in Liupan Mountain area in summer and autumn. *J. Meteorol. Environ.* **2019**, *35*, 28–37. (In Chinese)
31. Heymsfield, A.J.; Bansemer, A.; Poellot, M.R.; Wood, N. Observations of ice microphysics through the melting layer. *J. Atmos. Sci.* **2015**, *72*, 2902–2928. [CrossRef]